remote sensing

MDPI

Article

Intercomparison of Cloud Vertical Structures over Four Different Sites of the Eastern Slope of the Tibetan Plateau in Summer Using Ka-Band Millimeter-Wave Radar Measurements

Xia Wan [1,2,3,4], Jiafeng Zheng [2], Rong Wan [1,*], Guirong Xu [1], Jianfeng Qin [5] and Lan Yi [6]

1 Hubei Key Laboratory for Heavy Rain Monitoring and Warning Research, Institute of Heavy Rain, China Meteorological Administration, Wuhan 430205, China; wanx@whihr.com.cn (X.W.); grxu@whihr.com.cn (G.X.)
2 School of Atmospheric Sciences, Chengdu University of Information Technology, Chengdu 610225, China; zjf1988@cuit.edu.cn
3 Key Laboratory of Atmosphere Sounding, China Meteorological Administration, Chengdu 610225, China
4 Heavy Rain and Drought-Flood Disasters in Plateau and Basin Key Laboratory of Sichuan Province, Chengdu 610072, China
5 Wuhan Meteorological Service, Wuhan 430040, China; qinjianfeng0919@sina.com
6 Ganzizhou Meteorological Service, Kangding 626000, China; maomaoyu56147@sina.com
* Correspondence: wanrong@whihr.com.cn

Abstract: The eastern slope of the Tibetan Plateau is a crucial corridor of water-vapor transport from the Tibetan Plateau to Eastern China. This is also a region with active cloud initiation, and the locally hatched cloud systems have a profound impact on the radiation budget and hydrological cycle over the downstream Sichuan Basin and the middle reach of the Yangtze River. It is noteworthy that there is a strong diversification in the characteristics and evolution of the ESTP cloud systems due to the complex terrain. Therefore, in this study, ground-based Ka-band millimeter-wave cloud radar measurements collected at the Ganzi (GZ), Litang (LT), Daocheng (DC), and Jiulong (JL) sites of the ESTP in 2019 were analyzed to compare the vertical structures of summer nonprecipitating clouds, including cloud occurrence frequency, radar reflectivity factor, cloud base height, cloud top height, and cloud thickness. The occurrence frequency exhibits two peaks on the ESTP with maximum values of ~20% (2–4 km) and 15% (7–9 km), respectively. The greatest (smallest) occurrence frequency occurs in the JL (GZ). The cloud occurrence frequency of all sites increases rapidly in the afternoon, and the occurrence frequency of the DC presents larger values at 2–4 km. In contrast, the occurrence frequency in the JL shows another increase from 2000 LT to midnight at 7–11 km. Stronger radar echoes occur most frequently in the LT at 5–7 km, and hydrometeor sizes and phase states vary dramatically in mixed-phase clouds. A small number of radar echoes occur at midnight in the JL. A characteristic bimodality of the cloud base height and top height for single-layer, double-layer, and triple-layer clouds was observed. Clouds show a higher base height in the GZ and higher top height in the JL. The ESTP is dominated by thin clouds with thicknesses of 200–400 m. The cloud base height, top height, and thickness exhibit an increase in the afternoon, and higher top height occurs more frequently from midnight to the next early morning in the JL because of its mountain-valley terrain.

Keywords: Ka-band millimeter-wave radar; cloud occurrence frequency; cloud vertical structure; eastern slope of Tibetan Plateau

Citation: Wan, X.; Zheng, J.; Wan, R.; Xu, G.; Qin, J.; Yi, L. Intercomparison of Cloud Vertical Structures over Four Different Sites of the Eastern Slope of the Tibetan Plateau in Summer Using Ka-Band Millimeter-Wave Radar Measurements. *Remote Sens.* **2022**, *14*, 3702. https://doi.org/10.3390/rs14153702

Academic Editor: Carmine Serio

Received: 14 June 2022
Accepted: 29 July 2022
Published: 2 August 2022

1. Introduction

The Tibetan Plateau (TP), known as the third pole of the world, is the highest and largest plateau in the world [1,2]. The TP plays a significant role in regulating the atmospheric circulation and modulating Asian climate [3–5]. Because of its high terrain elevation, the observation of clouds over the TP and its vicinity heavily relies on passive satellite instruments, and various studies have been conducted to investigate cloud formation

mechanisms, spatial distributions, and temporal variations in this region [6–12]. Results from CloudSat and Cloud–Aerosol Lidar and Infrared Pathfinder Satellite Observations (CALIPSO) data revealed that deep convections over the TP are usually embedded in small-scale convective systems and are shallower than convections over the monsoon region in South Asia. However, the top layer of deep convective clouds over the TP is higher than that in other regions [8]. Based on the Tropical Rainfall Measuring Mission (TRMM) data, Qie et al., found that the intensity of deep convection over the TP is relatively weak, with lower vertical extension and smaller horizontal scale [9]. By using CloudSat/CALIPSO satellite measurements and TRMM precipitation products, relationships between cloud properties, radiative heating, and precipitation for convective and stratiform clouds in summer over the TP were analyzed and compared with counterparts in its neighboring areas [10]. The precipitation intensity caused by convective clouds is twofold stronger than that by stratiform clouds. The atmospheric shortwave (longwave) heating (cooling) rate strengthens with increased precipitation for both cloud types. The longwave cooling layer is thicker when the rainfall rate is less than 100 mm d^{-1}, while the net heating layer is typically compressed for the profiles of both cloud types over the TP. The cirrus formation mechanisms over the TP were also investigated by using CALIPSO data [11]. Large-scale orographic uplift, ice particle generation caused by temperature fluctuation, and remnants of overflows from deep convective anvils are considered three kinds of cirrus formation mechanisms over the TP. These three kinds of formation mechanisms occur at less than 9 km, between 9 km and 12 km, and above 12 km, respectively.

Even though satellite observations explored unique cloud properties over the TP, there are still some limitations in existence. The passive satellite sensors can make large-scale observations of clouds, and tend to miss optically thin clouds due to their low spatial resolution [13,14]. For example, CloudSat and CALIPSO (polar-orbiting satellites) make observations at approximately 1330 and 0130 local time, and probably miss the peak of the cloud's diurnal cycle [15,16]. Meanwhile, the TRMM product misidentifies weak convective rain events over the TP, because the freezing level is close to the surface in high-altitude regions [17]. Additionally, the accuracy of cloud top height (CTH) retrieval decreases with terrain height, by using the Fengyun-4A (FY-4A) and Himawari-8 satellites [18]. Take Himawari-8 for instance, the location of the TP is farther away from the subsatellite point of the Himawari-8. This longer distance results in a greater contribution from the path accumulation to the radiance, which causes an overestimation of the infrared brightness temperature and increases the difficulty in distinguishing the cloud from the surface.

In contrast, ground-based, vertical-pointing remote sensors (e.g., lidar, ceilometer, microwave radiometer, and millimeter-wave cloud radar) can provide cloud vertical structures with a higher spatiotemporal resolution and lower uncertainties. Therefore, many comprehensive field experiments equipped with multitype instruments were deployed over the TP in the past two decades. Among these observations, Qinghai-Xizang Plateau Meteorological Experiment (QXPMEX), the second Tibetan Plateau Atmospheric Experiment (TIPEXII), and the third Tibetan Plateau Atmospheric Experiment (TIPEXIII) are considered to be the most representative ones that featured such sensors [19–26]. By using the millimeter-wave cloud radar and microwave radiometer, Zhao et al. pointed out that the liquid cloud droplet and liquid water content both increase with height in July, which implied that more liquid water condensed in higher-altitude regions [22]. By combining the satellites (TRMM, CloudSat, and Aqua) with the ground-based radars (C-band radar and Ka-band radar), Wang et al. revealed the detailed microphysical processes in deep convective clouds over the TP [23]. The mixed-phase process and glaciated process mainly occurred in deep convective clouds. Furthermore, the mixed-phase process is different in deep strong convective clouds and deep weak convective clouds, respectively. For deep strong convective clouds, the rimming process occurs below the −25 °C isotherm, then the aggregation and deposition processes appear above the −25 °C isotherm, while this temperature threshold drops to −29 °C in deep weak convective clouds.

Currently, by using satellite data, most studies have examined the large-scale cloud characteristics over the main body of the TP. For the ground-based observations, analysis chiefly focused on the cloud vertical structures at the central TP (in Nagqu) [22–24], as well as convective activities and precipitation of the southern TP [8–10]. However, there is a lack of attention on the cloud vertical structure and diurnal statistical analysis on the eastern slope of the TP (ESTP). Clouds over the ESTP can evolve and eventually form heavy precipitation, which has a profound impact on the Sichuan Basin and the middle reach of the Yangtze River [27]. Geographically, the ESTP is a transitional area between the main body of the TP and the downstream Sichuan Basin. It is also a crucial corridor for the eastward water-vapor transport from the TP. In addition, the ESTP is near the Asian monsoon region and is dominated by a special circulation system induced by steep topography and complex terrains. Under this condition, the water-vapor distribution and internal circulation are cross-scale in the area, which makes it conducive to localized cloud formation. Owing to data limitations for this complex region, knowledge of cloud characteristics on the ESTP remains insufficient. Therefore, multisite ground-based observations with high spatiotemporal resolution on the ESTP are synthesized and analyzed in this study. These observations will help understand regional cloud characteristics on the ESTP, providing an observational basis and constrains for the potential improvement of numerical weather forecast models.

In monsoon summer during June and August in 2019, with joint support from the National Natural Science Foundation of China and the Institute of Heavy Rain, China Meteorological Administration, a field experiment on clouds and precipitation observations was conducted on the ESTP [28]. In this experiment, a Ka-band millimeter-wave cloud radar (Ka-MMCR), an X-band dual-polarization radar, a wind profile radar, and a microwave radiometer, were deployed at the meteorological station of Ganzi (GZ), Litang (LT), Daocheng (DC), and Jiulong (JL), respectively. The purpose of this experiment was to provide cloud properties over the ESTP from these ground-based observation instruments.

As shown in Figure 1, the four observation sites lie on the steep ESTP, which is the junction between the main body of the plateau and the downstream Sichuan Basin. The observation region (denoted by the red dotted rectangle) slopes from northwest to southeast in the ESTP, with high mountains and deep valleys staggered. Topographically, the GZ [31.62°N, 100.00°E, 3395 m above sea level (ASL)] is located in the northern part of the observation region, and is relatively close to the central TP. The GZ lies in a flat valley between the mountains, with the underlying surface of deep meadows. The LT (30.00°N, 100.27°E, 3951 m ASL) and DC (29.05°N, 100.30°E, 3727 m ASL) are located on the mountains concentrating around the southeastern edge of the TP, east of the Jinsha River [7]. The relative humidity in the LT and DC might be much higher than that in the GZ, due to the accumulation of water vapor in the mountain areas. The JL (29.00°N, 101.50°E, 2925 m ASL) is located in the southeastern part of the observation region. It possesses a mountain-valley terrain with a large altitude gradient and is the main source of the China southwest vortex [29]. These four-site observations with different topographic features provided a chance to investigate the characteristics of regional cloud systems and developments on the ESTP during the boreal summer in 2019.

Based on the four-site Ka-MMCR observations over the ESTP, this study statistically analyzed the vertical distribution and diurnal variation of cloud occurrence frequency, radar reflectivity factor, cloud base height (CBH), CTH, and cloud thickness. The remainder of this paper is organized as follows: In Section 2, the instruments, data, and method are described. Section 3 exhibits the statistical results of the cloud occurrence frequency, radar reflectivity factor, CBH, CTH, cloud thickness, and their diurnal variations. Discussions on the results are presented in Section 4. Conclusions are drawn in Section 5.

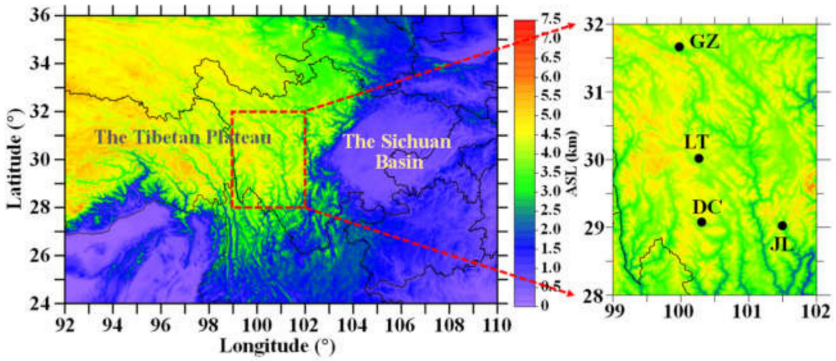

Figure 1. The geographic position and terrain of the four observation sites.

2. Data and Methodology

2.1. Radar Observations and ERA5 Reanalysis Data

To continuously obtain the aloft clouds, the zenith Ka-MMCRs manufactured by the Sun Create Electronics Co., Ltd. of China were employed at the GZ, LT, DC, and JL, respectively. All radars work at 35 GHz, with a wavelength of 8.6 mm and a beamwidth of 0.3°. The radars can provide vertical profiles of the reflectivity factor (Z_e, dBZ), mean Doppler velocity (V_M, m s^{-1}), spectrum width (σ_V, m s^{-1}), the linear depolarization ratio (LDR, dB), and Doppler spectra up to 20 km above the ground with a spatial resolution of 30 m and a temporal resolution of 10 s. Three operation modes are designed in Ka-MMCR to observe clouds at different altitudes [30]. In addition, the four Ka-MMCRs calibrations were accomplished before the field experiment. Take the radar calibration in the GZ for instance: external signal source ranging from −90 dBm to −40 dBm was input to the radar receiver, to obtain the values of Z_e at the height of 1 km. Meanwhile, the values of Z_e were calculated by the meteorological radar equation, based on the constants and measured parameters. Maximum difference of Z_e of copolarization channel is 0.47 dB, and maximum difference of Z_e of quadrature polarization channel is 0.94 dB. Intensive cloud observations were simultaneously conducted at the four observation sites from 5 June to 20 August 2019.

The atmospheric circulation patterns over the sampling region were analyzed based on ERA5 reanalysis products (https://cds.climate.copernicus.eu/cdsapp#!/search?Text=ERA5 (1 January 2022) of a 0.25° × 0.25° spatial resolution, hourly data on pressure levels from 1979 to the present. To reach the temporal consistency, hourly ERA5 data during the observation period were matched to the ground-based Ka-MMCR observation. The temperature and moisture profiles were supplied by the reanalysis products, to reveal the regional atmospheric conditions of the observational region.

2.2. Radar Data Quality Control

During the observation, both cloud echoes and nonmeteorological echoes were totally included in the radar reflectivity factor. In the low- and mid-latitude regions, nonmeteorological echoes observed by Ka-MMCR are mostly caused by low-level plankton, which consists of dust, insects, pollen, and other targets [31,32]. Plankton targets are mainly present within the planetary boundary layer and can affect the data usage of Ka-MMCR. Due to the existence of the nonmeteorological echoes, CBH is underestimated with uncertainties. For separation of the plankton contamination from the radar dataset, Z_e and LDR probability distributions of plankton and clouds were investigated [33]. According to the method from a previous study in Nagqu, the nonmeteorological echoes contribute to radar-measured Z_e with a value less than 0 dBZ and LDR with a value larger than −16 dB [34]. Herein, the algorithm was adopted to separate the nonmeteorological echoes in this study.

In addition, radar range sidelobes also should be filtered before the statistical analysis. To detect middle- and high-level clouds, the wide pulses and the pulse compression technologies are used in Ka-MMCR, which results in the range sidelobes. These artifacts

prevail near regions of clouds that contain great values of reflectivity factor and Doppler velocity in the radial direction [35]. The presence of these artifacts results in apparent smearing of echo from intense cloud echoes into the data of the adjacent height gates, which will further obstruct the retrieval of cloud macroscopic parameters, such as CBH (underestimated) and the CTH (overestimated). For vertical-pointing radars, the range sidelobe clutters will probably present above the top or below the base of the strong clouds with great values of reflectivity factor. In the study, the range sidelobe clutters are removed using Moran's method [35].

To present the effect of the radar data quality control, a typical case that contains non-meteorological echoes and range sidelobe clutters is plotted in Figure 2. The observation exhibits that clouds successively moved over the Ka-MMCR deployed in the LT on 9 July 2019. In Figure 2a, the clouds are surrounded by nonmeteorological echoes (denoted by red arrows) and are seriously impacted by the range sidelobe clutters (denoted by black arrows). The nonmeteorological echoes were concentrated on the low-level lower atmosphere, occurring at the height of 0–1 km around 0700–1400 local time (LT). These echoes were frequently mistaken for fractus near the ground, which brings an obstacle to cloud layer detection. Meanwhile, relatively more intensive clouds with greater radar echoes approaching 30 dBZ developed, and the clouds were confused by the range sidelobes (marked by black arrows) during 0900–2000 LT, which were determined by the Moran's criterion. On one hand, range sidelobes (0900–1400 LT) lying at the cloud bottom present a reflectivity value of ~−25 dBZ, around 45 dB smaller than the strong echo core (20 dBZ) in clouds at the height of ~4.5 km. On the other hand, range sidelobes (1400–2000 LT) connecting with the cloud top show a reflectivity value of ~−20 dBZ, around 50 dB smaller than the strong echo core (30 dBZ) in clouds near the ground. Furtherly, the existing range sidelobes in between 1400–1500 LT fuzz the boundaries of adjacent cloud layers, which might cause errors in the following statistics of the CBH, CTH, and cloud thickness. As shown in Figure 2b, the scattered nonmeteorological targets were well-eliminated after the quality control, and the range sidelobe clutters were also removed.

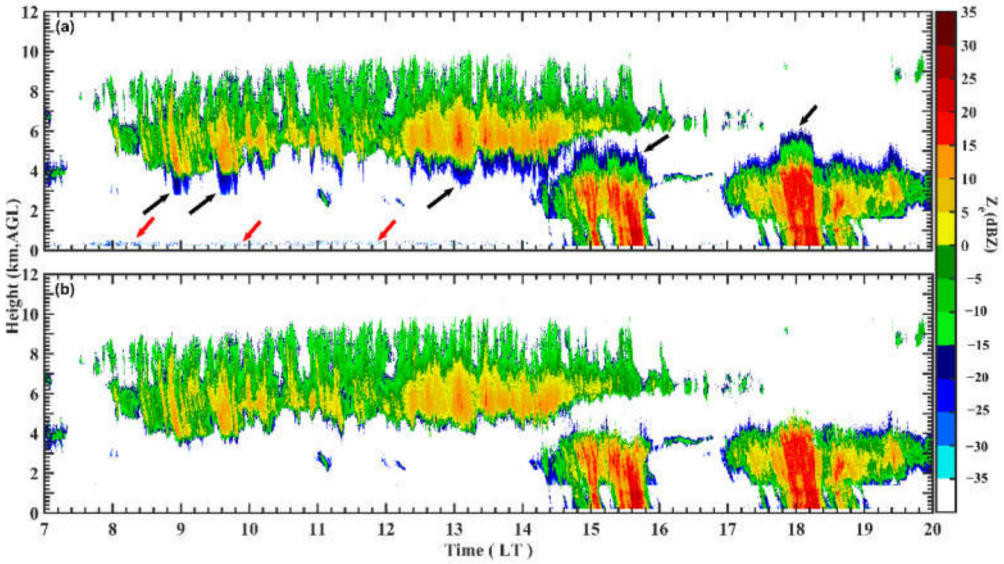

Figure 2. The time-height cross sections of radar original reflectivity factors (Z_e, dBZ) (**a**), and the reflectivity factors after quality control (**b**), as observed by Ka-MMCR at the LT site on 9 July 2019.

2.3. Profile Classification

Millimeter-wavelength signals are usually used to detect the small-size hydrometeors in clouds, and the occurrence of precipitation on the ESTP could lead to strong attenuation of the Ka-MMCR signal [36,37]. Because of the presence of precipitation, the cloud top height obtained by the Ka-MMCR tends to be lower than reality [38]. Meanwhile, the

bottom of precipitating clouds is close to the surface, and it is difficult to verify the cloud base height using the Ka-MMCR. In general, important parameters (e.g., cloud base height and top height) during the cloud formation and development stages will be inaccurately detected by the Ka-MMCR with collocated rainfall. Therefore, nonprecipitating clouds observed by Ka-MMCR are focused in this statistical analysis. The non-precipitating cloud profiles were identified and selected from the total radar profiles by the following steps. First, the entire radar profiles were divided into two categories, namely the cloud profiles and the clear-sky profiles. A profile was defined as the cloud profile when the radar echo includes hydrometeors; otherwise, it was treated as the clear-sky profile. Subsequently, the cloud profiles were further classified into two types—the nonprecipitating cloud profile and the precipitating cloud profile—by judging if the simultaneous ground rain rate (observed by the collocated surface disdrometers) was greater than 0.01 mm h^{-1}.

After the classification, different types of sample profiles from the four observation sites are summarized in Table 1. The N_c is the number of cloud profiles, the N_{npc} is the number of nonprecipitating cloud profiles and the N_{total} is the total number of all sample profiles. Statistics show that a total of 276,480 profiles (N_{total}) were observed by the Ka-MMCR at each observation site from 5 June to 20 August 2019. From all the here-analyzed observations, both the largest N_c (144,892) and N_{npc} (121,934) were observed in the JL.

Table 1. The Ka-MMCR dataset samples at four sites from 5 June to 20 August 2019.

Site	Latitude	Longitude	Altitude	N_{total}	N_c	N_{npc}
GZ	31.62°N	100.00°E	3395 m	276,480	104,881	87,978
LT	30.00°N	100.27°E	3951 m	276,480	114,047	104,316
DC	29.05°N	100.30°E	3727 m	276,480	138,596	113,490
JL	29.00°N	101.50°E	2925 m	276,480	144,892	121,938

3. Results

3.1. Cloud Occurrence Frequency

Cloud occurrence frequency refers to the height-resolved distributions of cloud occurrence measured by the Ka-MMCRs. This analysis is carried out on the nonprecipitating cloud profiles. Hence, the cloud occurrence frequency is calculated as the ratio of the number of nonprecipitating cloud profiles (N_{npc}) to the total number of the observed profiles (N_{total}).

Figure 3 shows the vertical distribution of cloud occurrences at four sites. Original profiles of cloud occurrence frequency are presented in Figure 3a, and smoothed profiles are presented in Figure 3b. Four original profiles roughly show a bimodal distribution, respectively. These profiles contain small values (5%–10%) below ~1.5 km, which are probably caused by a small amount of clouds in the low-level atmosphere. To unravel the overall trends of the distribution of nonprecipitating clouds with different underlying surfaces, these profiles are smoothed. As shown in Figure 3b, there are two peaks located at the height of 2–4 km (main peak) and 7–9 km (secondary peak), respectively. This finding is in good agreement with the studies in the Nagqu: the values of cloud occurrence frequency show two peaks (located at 2–4 km and 6–9 km separately) in summer [39]. Nevertheless, the four-site observations on the ESTP display significant regional differences in occurrence frequency peak values and locations. The results show that maximum values (main peak) of occurrence frequency in the DC and JL are ~20%, which is significantly larger than in the LT and GZ. Conversely, the main peak location of occurrence frequency in the GZ is higher than 3.5 km, which is slightly higher than in other sites. Meanwhile, the maximum value (secondary peak) of occurrence frequency in the JL is larger than 15%, which is dramatically larger than in other three sites. The secondary peak location of occurrence frequency in the JL is higher than the counterparts of the other sites, with the height of 8.5 km. In general, the occurrence frequency in the JL is larger than in other sites, with the cloudiest conditions

among the four observation sites. Meanwhile, the occurrence frequency in the GZ is the smallest, which indicates that cloud formation in this region is relatively difficult.

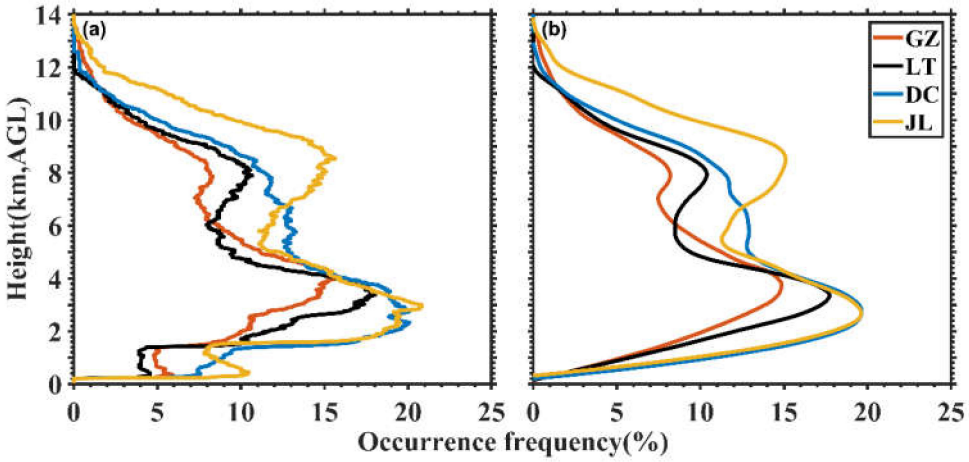

Figure 3. Vertical distributions of cloud occurrences at four sites. Original profiles of cloud occurrence frequency (**a**), and smoothed profiles of cloud occurrence frequency (**b**), as calculated by Ka-MMCR observations.

The ESTP is the submaximum elevation-gradient region of China, and strong ascending motion occurs in this region due to the topographic forcing and the upslope mountain-valley circulation [12,40]. Among the four observation sites, the JL (2925 m, AGL) is located in the canyon, with the largest altitude gradient. Deep-cut rivers flow from north to south in this region, and the rivers play an important role in guiding water-vapor transport. Thereby, more warm and humid airflow can facilitate the cloud formations in the JL. This supports the Ka-MMCR observations that the highest cloud occurrences occur both in the low-level and high-level troposphere in the JL. In contrast, the water-vapor amount in the GZ is relatively insufficient, because the moisture airflow splits into several branches during the transport. Meanwhile, the vertical movement of airflow becomes weak due to the decreasing altitude gradient in the GZ (3395 m, AGL). Under this condition, the occurrence frequency in this region presents the smallest values. These may suggest that the local underlying surface plays an important role in controlling the occurrence of the clouds. To further understand the regional differences in cloud occurrence frequency on the ESTP, the patterns of moisture convergence at four sites will be analyzed in Section 4 in detail.

To describe the cloud diurnal variations at four sites, the cloud occurrence frequency is calculated every 60 min with 30 m vertical resolution. Figure 4a–d show the temporally normalized values of cloud occurrence frequency at different AGL heights. Figure 4e presents the hourly changes of cloud occurrence frequency, which is the summation of the occurrence frequency of all heights within 60 min. Regional differences in cloud occurrence are apparent throughout the day. In the DC, observations show two cloud layers, associated with the diurnal cycle and convective instability. In the lower layer, the maximum occurrence frequency (2%) is observed between 1200 LT and 1800 LT at an altitude extending from ~0.5 km to 5 km. In the upper layer, the maximum value of occurrence frequency (1%) is located at 7–10 km during 1600 LT and 1900 LT, which probably corresponds to deep convective clouds. The occurrence frequency in the JL shows a similar diurnal distribution to the DC, whereas in the lower layer, the maximum value of occurrence frequency (2%) in the JL presents a shorter period (1300–1500 LT), and is located at 3–4 km. In the upper layer, the maximum occurrence frequency (1%) in the JL is observed from 1600 LT to the early morning. In the LT site, observations show only a lower cloud layer; the maximum value of occurrence frequency (2%) is observed between 1500 LT and 1600 LT at an altitude extending from ~4 km to 5 km. In contrast, the occurrence

frequency in the GZ shows unapparent variation, with the maximum value of occurrence frequency (1%) smaller than other sites. Previous studies showed that diurnal differences in the intensity of convection have a significant impact on the cloud diurnal variations [41,42]. The TP is a heat source in summer, enhances the surface heating, and further enhances the convections over the TP [43,44]. Surface heating from solar radiation causes instability at lower levels, which leads to moist convection and cloud formation [45]. Under this condition, cloud occurrence frequency sharply increased in the afternoon. Furthermore, cloud occurrence frequency of the four sites does not increase at the same time due to the regional triggering time of convective processes [46]. Figure 4e shows that the occurrence frequency of the four sites increases rapidly in the afternoon (1300–1800 LT), then decreases slowly in the morning (0000–0500 LT), and reaches a minimum value around 1030 LT. In Figure 4e, the hourly occurrence frequency of clouds in the LT site begins to increase around 1030 LT earlier than other sites, probably because the convective process in the LT is triggered firstly among the four observation sites. On the other hand, cloud occurrence frequency in the JL shows a sudden increase at midnight, which is associated with the occurrence frequency increase at 7–11 km (Figure 4d). The results are similar to the findings from Zhou et al. [47], which reported that cloud occurrence frequency of the southern TP (e.g., Motuo) remained near the maximum value (40%) from evening to midnight, then decreased rapidly in the morning. The maximum values of occurrence frequency throughout the day in the DC, JL, LT, and GZ are 78%, 70%, 55%, and 50%, respectively. Nonprecipitating clouds form more frequently on the ESTP than on the southern TP.

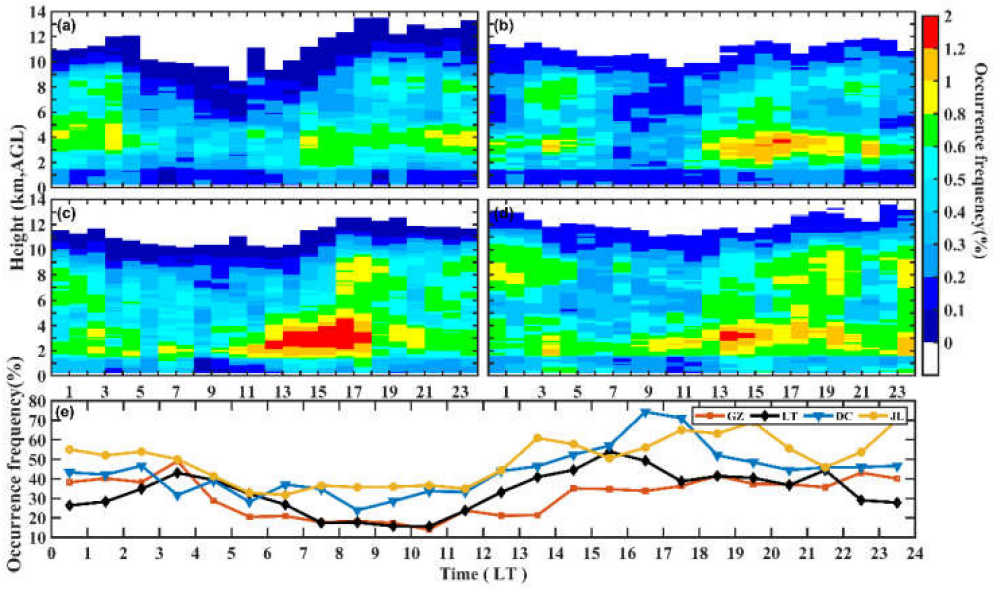

Figure 4. Diurnal variations of cloud occurrence frequency at four sites. (**a**) GZ; (**b**) LT; (**c**) DC; (**d**) JL; (**e**) hourly changes of cloud occurrence frequency.

3.2. Radar Reflectivity Factor

The radar reflectivity factor (Z_e) measured by Ka-MMCR can represent the distribution of hydrometeor size and concentration in nonprecipitating clouds. According to the meteorological radar equation [48], the size and phase state (liquid/mixed/ice phase) of hydrometeors can directly affect the value of Z_e. Particularly, hydrometeors with large diameters in clouds contribute to the great values of Z_e. Great values of Z_e are related to strong clouds, and narrow variation ranges of Z_e represent good consistency of hydrometeor size and concentration in clouds. More importantly, the temperature is a key factor of hydrometeor phase states, and regional temperature changes have an impact on the cloud intensity. Figure 5 shows the gradient changes of mean temperature from ERA5 reanalysis data in four sites between 5 June and 20 August in 2019. The temperatures decrease linearly with increasing altitudes among four sites, then the 0 °C isotherm and

the −40 °C isotherm are located in between at altitudes of ~1.6–2.6 km and ~7.8–8.8 km, respectively. Furthermore, studies have shown that hydrometeors exist as liquid water in clouds above 0 °C, mixed-phase clouds (including supercooled water and ice crystal) might stay from 0 °C down to −40 °C, and nearly pure ice clouds (including ice crystals) are located in the high-level atmosphere below −40 °C [49].

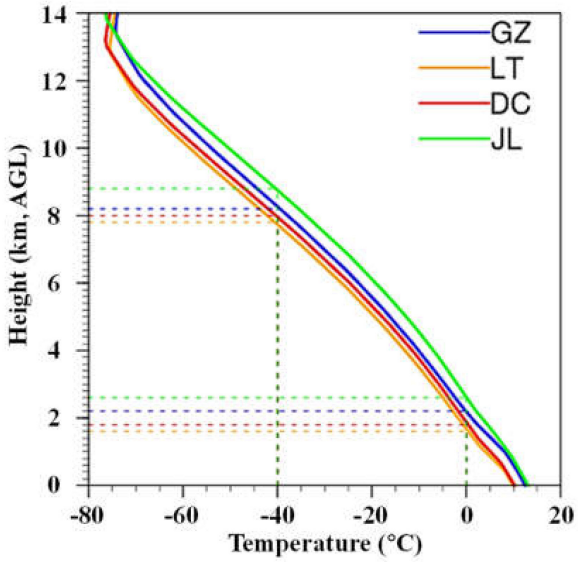

Figure 5. The vertical temperature gradient changes from ERA5 at four sites.

As shown in Figure 6, the height-resolved variations of Z_e are calculated in boxplots (Figure 6a–d), and the mean value profiles of Z_e are superimposed (Figure 6e). Significantly, the mean values of Z_e are calculated in log scale. Boxes denote the 25th and 75th percentile positions, whereas the lines and dots inside the box show the median and mean values, respectively. To ensure that each layer has samples for statistical robustness, the data were resampled to a vertical resolution of 500 m. The boxplots of Z_e for non-precipitating clouds differ remarkably among the four observation sites. Above the height of −40 °C isotherm (~9 km), the values of Z_e range from −25 dBZ to −5 dBZ. With the height decrease, the values of Z_e of four sites firstly exhibit a slight increase, then present a rapid decrease. Compared to the same height in other sites, the boxes cover a wider dBZ range in the GZ (Figure 6a). In between the height of 0–−40 °C isotherm (~1.7–9 km), the values of Z_e increase rapidly with the altitude decrease and reach the maxima of ~−10 dBZ at 5–7 km. During this process, the radar reflectivity factors present a wider range, which probably indicate that particle size and concentration in clouds varies significantly among the four sites. In between the height of ~2–6 km, the values of Z_e decrease with the height decrease. Meanwhile, the boxplots cover a narrower dBZ range in the GZ, LT, and JL, while the dBZ range becomes wider in the DC (Figure 6c). The values of Z_e maximize (−10–−5 dBZ) below of ~0 °C isotherm (~2 km), which suggests that particles in clouds began to melt in this layer. Below ~1.5 km, the values of Z_e start to decrease rapidly. As shown in Figure 6e, the mean values of Z_e of four sites present the peak values at 5–7 km. In between the height of 5–7 km, the maximum value of mean Z_e in the LT is larger than that of other sites, while the maximum value of mean Z_e in the GZ is smallest. In other words, mixed-phase clouds at 5–7 km present relatively stronger in the vertical direction. Among the four observation sites, nonprecipitating clouds in the LT are the strongest.

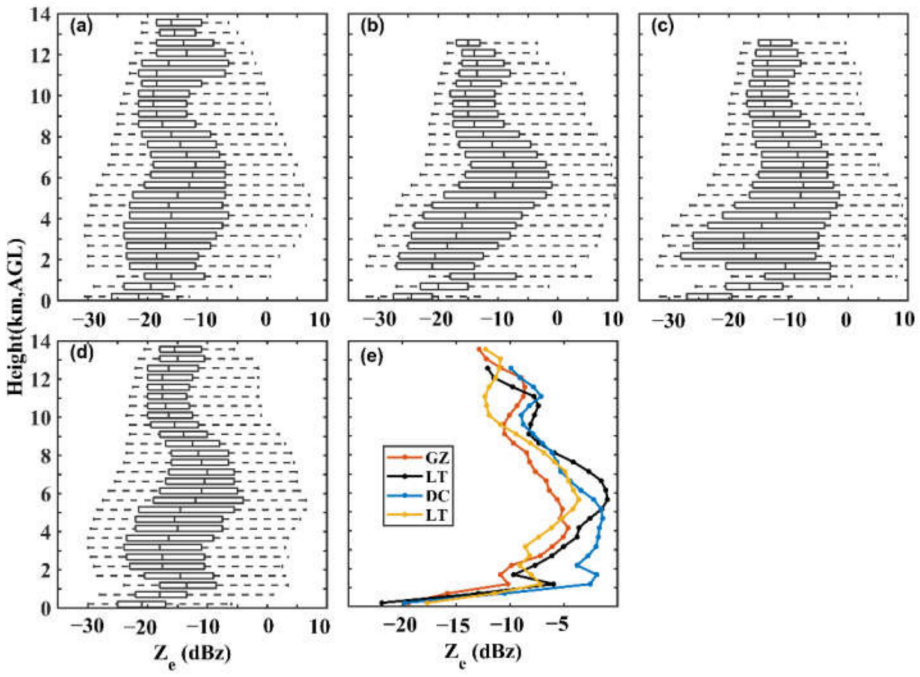

Figure 6. Vertical distributions of the radar reflectivity factor (Z_e) at four sites. In box and whisker plots, the left and right lines of each box represent the 25% and 75% values, respectively, and the gray solid line inside the box indicates the median position. (**a**) GZ; (**b**) LT; (**c**) DC; (**d**) JL; (**e**) mean values of Z_e.

To better understand the daily distribution of radar echoes at four sites, mean Z_e of log scale is calculated every 60 min with 30 m vertical resolution. Figure 7a–d present the height-resolved temporal evolutions of mean Z_e at different AGL heights. Figure 7e shows the hourly changes of mean values of Z_e, which are the mean values of Z_e of all AGL heights within 60 min. As shown in Figure 7b, the maximum Z_e (~10 dBZ) occurs in the morning (0500–0800 LT), and in the afternoon to night (1800–2300 LT) in the LT site. The radar echoes with maximum value in the afternoon are mainly located at 5–7 km, which is consistent with the result of the LT site in Figure 6e. Similarly in Figure 7a, radar echoes in the GZ exhibit maximum value (~10 dBZ) in the morning (0600–0800 LT), in the afternoon (1400–1500 LT), and at night (2200–2300 LT). In the DC, the maximum Z_e (~10 dBZ) occurs in the afternoon (1700–1800 LT), with the height of 2–5 km (Figure 7c). In the JL, radar echoes with maximum value (~10 dBZ) occur in the afternoon (1600–1900 LT) at 1–2 km, and in the midnight (0000–0100 LT) at 6–7 km, respectively. Importantly, large values (0 dBZ) of Z_e at four sites occur in the afternoon, which is most probably associated with the convective processes [43,44]. From the Ka-MMCR observations, strong radar echoes mainly consist of ice crystal, because these clouds are located in between the height of 0−−40 °C isotherm. These results show that hydrometeor sizes and phase states vary dramatically in mixed-phase clouds on the ESTP, and the localized convections induce more complicated microphysics processes at four sites. Generally, the large values of Z_e are caused by the strengthening of mixed-phase clouds. In Figure 7e, mean values of Z_e increase in the afternoon, and maximize around 1500–1700 LT, then decrease from the night to the next morning. The minimum values occur around 1030 LT, which is consistent with the valley value occurrence of cloud occurrence frequency (see Figure 4e).

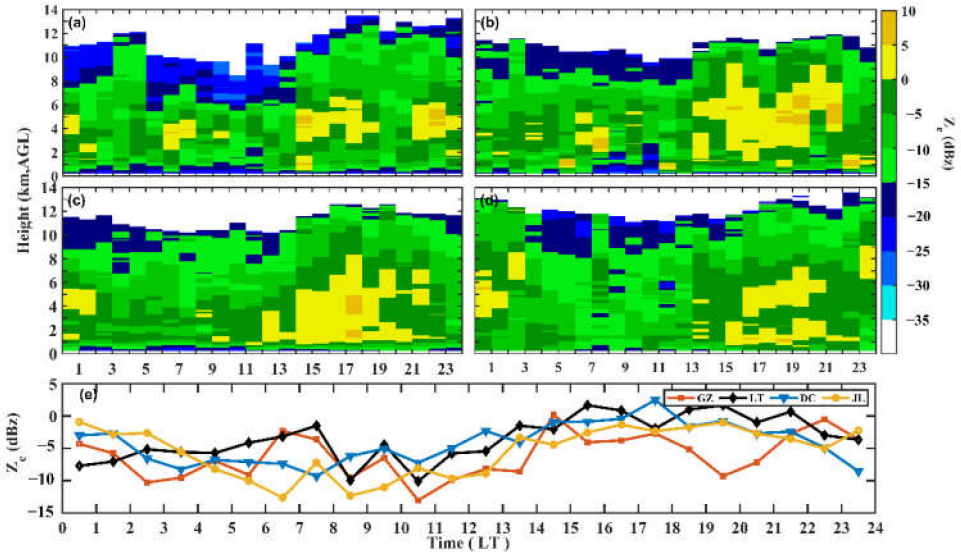

Figure 7. Diurnal variations of the radar reflectivity factor (Z_e) at four sites. (**a**) GZ; (**b**) LT; (**c**) DC; (**d**) JL; (**e**) hourly changes of mean values of Z_e.

3.3. Cloud Macroscopic Parameters

Cloud macroscopic parameters measured by cloud radars, such as the CBH, CTH, and cloud thickness, are widely used to analyze the cloud vertical structures in recent years [38,47,50,51]. To verify the reliability of these parameters measured by the cloud radar, previous studies have compared the CBH (CTH) from the cloud radar with the ceilometer (FY-4A) and found a relatively high consistency between the two datasets [44,46]. In addition, the four Ka-MMCRs used in this study were well-calibrated before the field experiment. In this work, CBH and CTH from the Ka-MMCRs are confirmed using Wu's method for cloud boundaries of the TP [51]. In Wu's method, the lower boundary of nonprecipitating clouds is defined as the CBH, and the upper boundary of nonprecipitating clouds is defined as the CTH, corresponding to the post-quality-control data. Herein, the cloud thickness is a geometrical thickness, which is defined as the difference between the top height and base height. In the vertical direction, cloud clusters overlapped with an interval less than 90 m are treated as the same-layered cloud; otherwise, they are different-layered clouds. Then, the thickness of each layer and the space between adjacent cloud layers are determined. From the previous analysis, clouds with a layer number of no more than three occur more frequently over the TP and the adjacent areas, with the maximum occurrence frequency larger than 95% [52,53]. Therefore, the CBH, CTH, and cloud thickness of the single-layer, double-layer, and triple-layer clouds from the radars are considered, and clouds with a layer number of more than three will be neglected in this section.

The height-resolved Ka-MMCR observations enable the determination of the spatial evolution of CBH, CTH, and cloud thickness. CBH is related to water-vapor condensation height; CTH and cloud thickness present cloud vertical extension. Significantly, the vertical distribution of these parameters can reveal regional cloud formation and development on the ESTP. The probability density function (PDF) profiles of the CBH, CTH, and cloud classification results are displayed in Figure 8. The definition of different cloud layers is also interpreted. Here, Layer-1, Layer-2, and Layer-3 present the lowest-layer clouds, middle-layer clouds, and highest-layer clouds, respectively. Because the clouds in low-level atmosphere have little impact on the bimodal distribution of clouds in the vertical direction at four sites (see Figure 3), the profiles of CBH and CTH are processed by fitting in Figure 8a–c,e–g. From all the here-analyzed observations, the CBH profiles of all layers present a bimodality in the vertical direction (Figure 8a–c). For the lowest-layer clouds, the main peaks of the CBH profiles are located at 1–4 km, and the secondary peaks of the

CBH profiles are located at 6–8 km. Note that the main peak of the CBH of the lowest-layer clouds in the GZ is higher by 1km than other sites. For the highest-layer clouds, the main peaks of CBH profiles are located at 7–10 km; particularly, the peak in the JL is higher by 1 km than in other sites. Meanwhile, different categories of clouds can be classified by the values of CBH. According to the cloud classification method proposed by the WMO [54], the CBH results are used to categorize the clouds as high (CBH $>$ 5 km), middle (2.5 km $\leq$ CBH $\leq$ 5 km), and low (CBH $<$ 2.5 km) clouds, as shown in Figure 8d. In the GZ, middle clouds occur most frequently (38%), then the occurrence frequency of low clouds and high clouds are 34% and 27%, respectively. Differently, low clouds occur most frequently both in the DC (46%) and the LT (38%), then middle clouds occur second-most frequently (35% in the LT, 29% in the DC), and the occurrences of high clouds are fewest (27% in the LT, 26% in the DC). In contrast, the occurrence frequency value of low clouds is maximum (39%) in the JL, followed by the high clouds (33%) and middle clouds (28%). Consistent with the CBH distributions, the CTH profiles play a bimodal pattern in the vertical direction (Figure 8e–g). For different layer clouds, the main peaks of CTH profiles in the GZ are located at 4.5–5 km, and the peaks are significantly higher than in other sites. Furthermore, the secondary peak of the CTH profile in the JL is located at ~10 km, and the peak is also apparently higher than in other sites. Clouds in the JL generally show a higher (~0.5 km) top height among the four sites, which suggests that a more drastic vertical air motion happened in this region in the 2019 summer.

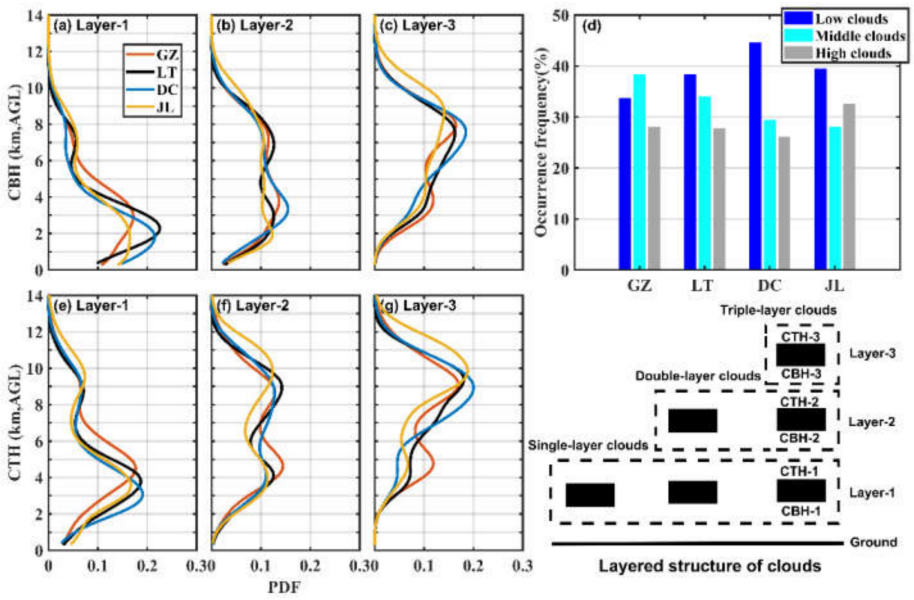

Figure 8. The PDF of the base height and top height from different layer clouds, and the result of cloud classification. (**a**–**c**) CBH; (**d**) clouds classification results; (**e**–**g**) CTH. (**a**,**e**) Layer-1; (**b**,**f**) Layer-2; (**c**,**g**) Layer-3.

PDF plots of the thickness of single-layer, double-layer, and triple-layer clouds are illustrated in Figure 9. The PDF profiles of all cloud layers show a unimodal distribution. As shown in Figure 9, the maximum value of the PDF corresponds to the central thickness. For the same observation site, the single-layer clouds exhibit a minimum value of PDF, the double-layer clouds present a second minimum value of PDF, and the triple-layer clouds show a maximum value of PDF (Figure 9a). Central thickness of single-layer clouds presents a maximum value, central thickness of double-layer clouds presents a second maximum value, and central thickness of triple-layer clouds presents a minimum value. Meanwhile, the thickness of single-layer clouds extends to ~8 km, the thickness of double-layer clouds extends to ~6.6 km, and the thickness of triple-layer clouds extends to ~6 km. Because of the increase in cloud layer number, the peak value of PDF increases, the central thickness

decreases, and the cloud thickness extension also decreases. In other words, clouds become thinner when the number of cloud layers increases, which is in good agreement with the compression effect of TP terrain on the vertical cloud structures reported by previous studies [10,52]. In general, the ESTP is dominated by thin clouds with thicknesses of 200–400 m. Among the four observation sites, the maximum value of PDF profiles in the LT is larger, and the cloud thickness exhibits smaller values. This result potentially shows that clouds in the LT are more strongly compressed by the high-altitude terrain.

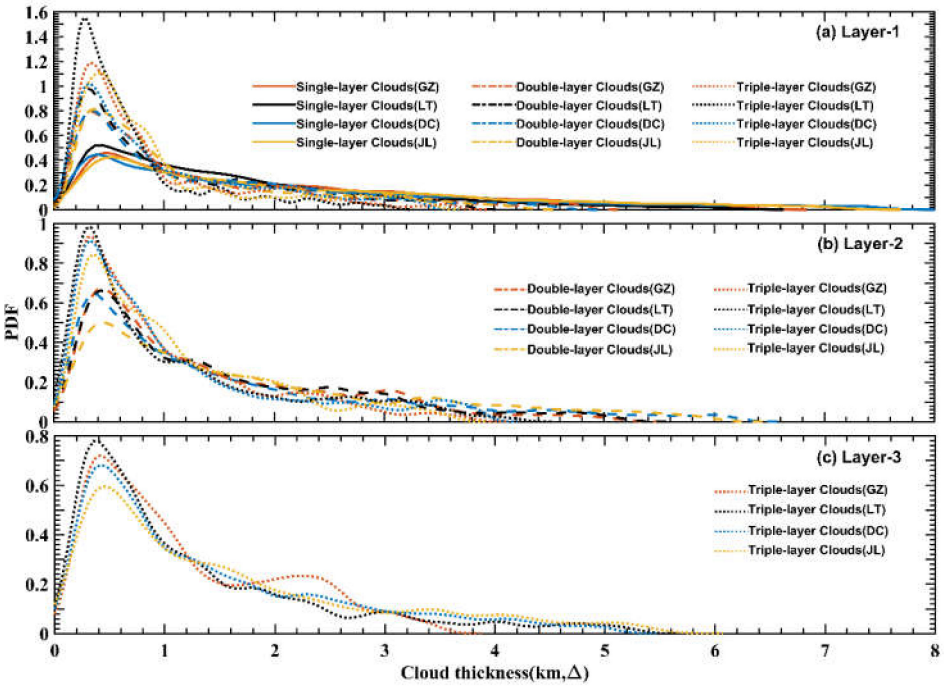

Figure 9. PDF plots of the thickness of single-layer, double-layer, and triple-layer clouds. (**a**) Layer-1; (**b**) Layer-2; (**c**) Layer-3.

To further investigate the diurnal variations of water-vapor condensation height and cloud vertical extension, diurnal evolutions of base height of the lowest-layer clouds (CBH-1), top height of the highest-layer clouds (CTH-3), and the thickness of CTH-3 and CBH-1 are displayed in Figure 10. Significantly, the base height of CBH-1 is closely associated with local underlying surface, and the top height of CTH-3 largely exhibit the localized cloud vertical extension. The data of CBH-1, CTH-3, and the thickness of CTH-3 and CBH-1 are calculated every 60 min with 30 m vertical resolution. Statistics show that 50% (25th–75th of the data included by the box) of the base heights range from 0.24 km to 6 km (Figure 10a,d,g,j). Cloud base heights in the GZ display a gentle decrease throughout the morning until ~1500 LT, and increase rapidly to the peak at around 2200 LT. In contrast, cloud base heights in the LT roughly show a bimodality during the day, with one peak from midnight to around 1300 LT and the other peak from the afternoon to the late night. In the JL, clouds exhibit much lower base heights in the middle night and early morning, which is likely associated with the warm and humid airflow. Compared with the base heights, 50% of top heights reveal a bimodal pattern ranging from 3 km to 10 km, with the peak during early morning and afternoon (Figure 8b,e,h,k). In the GZ, one peak of top height occurs at 1900–2100 LT and the other peak occurs at 0200–0400 LT. The diurnal variation of top heights in the LT is similar to that in the GZ, with the peak values in the early morning (0300–0400 LT) and late night (2000–2300 LT). The peaks of top heights in the DC occur during 0000–0300 LT and 1500–2000 LT. In the JL, cloud top heights show a minimum value at 1200 LT, rapidly increase during 1300–1700 LT, and maximize at 2000 LT, then drop from the night to the early morning. Significantly, higher cloud top heights occur more frequently from midnight to the next early morning in the JL, which might be

correlated with the collision of the up-valley wind from summer monsoon airflow with the down-valley wind [55]. Interestingly, the observations show that cloud top heights increase earlier than the base heights increase in the afternoon, and the diurnal variation of cloud top heights are more significant than those of base heights. The daily changes in the thickness are similar to the evolution of top heights, with two peaks in the afternoon and early morning, respectively (Figure 10c,f,i,l). It is most probable that the convectively unstable atmosphere might thereby thicken the clouds. These results are generally in good agreement with previous finds from radiosondes on the ESTP and other regions in China [56].

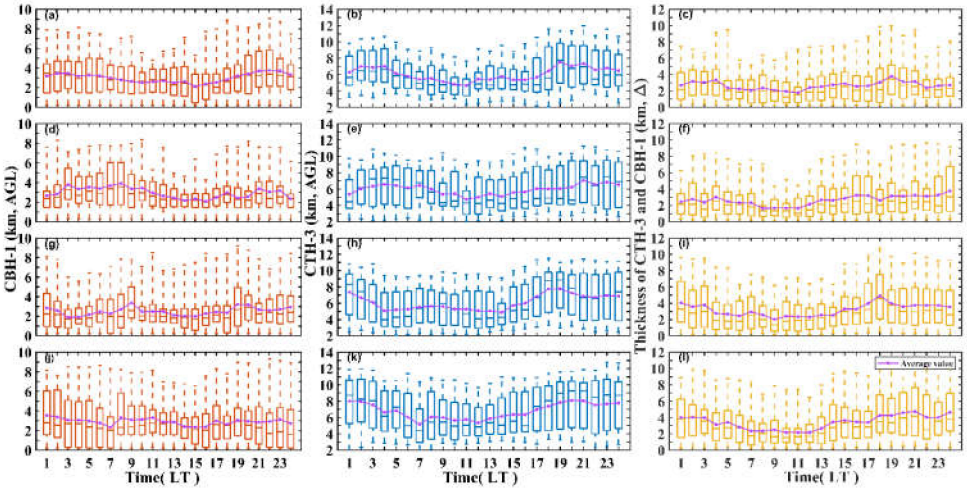

Figure 10. Diurnal variations of base height of the lowest-layer clouds (CBH-1), top height of the highest-layer clouds (CTH-3), and the thickness of CTH-3 and CBH-1 at four sites. In box and whisker plots, the upper and lower lines of each box represent the 75% and 25% values, respectively, and the red/blue/yellow solid line inside the box indicates the median position. (**a**,**d**,**g**,**j**) CBH-1; (**b**,**e**,**h**,**k**) CTH-3; (**c**,**f**,**i**,**l**) thickness of CTH-3 and CBH-1. (**a**–**c**) GZ; (**d**–**f**) LT; (**g**–**i**) DC; (**j**–**l**) JL.

4. Discussion and Comparison

The ESTP region is well-known to act as a convergence zone during the summer monsoon [44]. Geographically, the ESTP is an important part of the TP and absorbs the solar radiation strongly. The large sensible heating in this region results in convergences, which form ascending movements throughout the day [57]. Therefore, local atmospheric circulation presents some differences in vertical and daily changes, which might impact the cloud properties of four-site observations on the ESTP.

For instance, the diurnal variation of cloud occurrence frequency is closely related to the diurnal cycle of the convergences. The airflow ascending movements caused by convergences are beneficial to the water-vapor condensation. Figure 11 shows the diurnal variations of moisture flux divergence at four sites. The values of moisture flux divergence are averagely calculated by the ERA5 reanalysis data every 60 min. Data interpolation is used in the vertical direction. The negative values of moisture flux divergence present convergence, and smaller negative values indicate stronger convergence. As shown in Figure 11b–d, the surrounding airflows converge (denoted by a negative contour value) near the surface in the LT, DC, and JL, from the afternoon to the evening. Strong convergences occur in the afternoon, aggravate the cloud process, and result in a great increase in occurrence frequency in these sites (see Figure 4b–d), respectively. The minimum value of moisture flux divergence ($<-30 \times 10^{-6}$ g/cm^2·hPa·s) in the DC and JL is smaller than in the LT, which indicates that stronger convergences happen in the first two sites. From the Ka-MMCR observations, the values of occurrence frequency in the DC and JL are larger than in the LT (see Figure 4e). In contrast, unapparent diurnal variation cycles of convergence occur in the GZ, which leads to unapparent variations in cloud occurrence

frequency throughout the whole day (see Figure 4a). Based on the early studies, the thermal forcing of heating increases the potential temperature of the air column, and the induced mechanical forcing results in convergence in lower levels but divergence in upper levels [58]. From the ERA5 reanalysis data in the JL, airflows diverge (denoted by a positive contour value) strongly above the convergence zone, with a maximum value of moisture flux divergence larger than 18×10^{-6}g/cm^2·hPa·s. Under this condition, the air ascending motion is strongly suppressed, which may weaken the local cloud formation process. Hence, from the observations, the occurrence frequency values of the lower troposphere in the JL are generally smaller than in the DC during the afternoon (see Figure 4c–d).

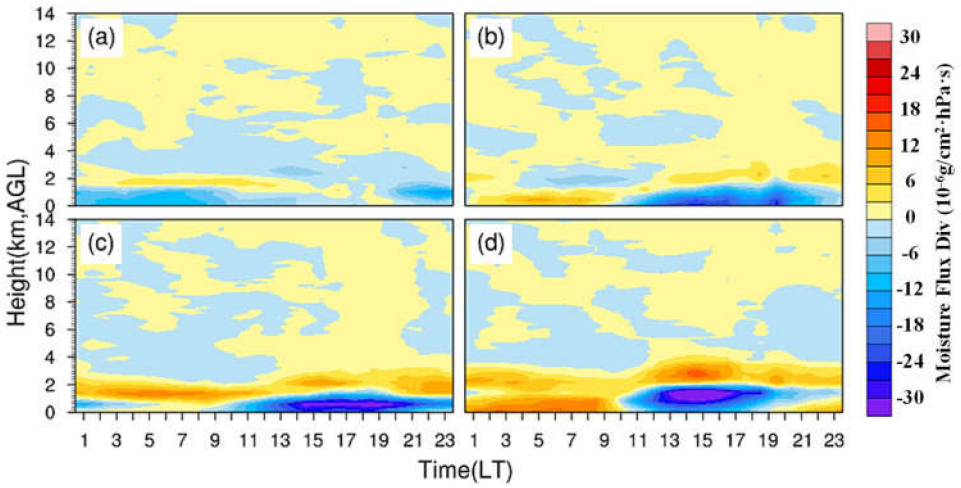

Figure 11. Diurnal variations of moisture flux divergence at four sites, as calculated by ERA5 reanalysis data. The negative values indicate airflow converge, and the positive values indicate airflow divergence. (**a**) GZ; (**b**) LT; (**c**) DC; (**d**) JL.

In general, unique cloud properties on the ESTP in summer are caused by the effects of topography, irradiation, and heat source [59]. Numerous studies show large differences in cloud vertical structures and diurnal variations between the ESTP and Eastern China. By using the Cloudsat/CALIPSO data, the distribution of hydrometeors also exhibits two peaks in summer in Eastern China [8]. The first peak is located in the upper troposphere, with the maximum value at higher altitudes (12–15 km) in Eastern China than that (7–9 km) in the ESTP (see Figure 3). The second peak is located at approximately the same height (1–3 km) in Eastern China as that (2–4 km) in the ESTP. For the distribution of dBZ for nonprecipitating clouds, the observations in Eastern China (e.g., Beijing) exhibit different vertical variations during summer [47]. Firstly, the dBZ values of clouds in Beijing are generally larger than that in the ESTP, with the maxima of ~40 dBZ (Beijing). The result shows that the clouds on the ESTP (adjacent region of the TP) are weaker than in other regions, which is consistent with the previous studies [8,9]. Secondly, the dBZ profile (mean value) of mixed-phase clouds present a linear decrease from ~9 km downwards to ~5 km (~0 °C isotherm) in Beijing. The observations on the ESTP (see Figure 5) show that the mean dBZ values of mixed-phase clouds rapidly maximize (−5–0 dBZ) in between the height of 6–9 km, and decrease to ~−9 dBZ at ~2 km (~0 °C isotherm). There are likely more complicated physical processes in mixed-phase clouds on the ESTP. In addition, the cloud occurrence frequency presents a sharp increase from 1500 LT in Beijing during summer and reaches the maxima (60%) in the early morning [60]. Due to the heat source of the TP in summer, cloud occurrence frequency of the ESTP exhibits a rapid increase around 1300 LT earlier than that in Beijing. Furthermore, the daily occurrence frequency of clouds shows a maximum of 80% larger than that in Beijing, which indicates ESTP has a higher water-vapor content in the summer [59].

However, there are still some uncertainties and limitations of the results, which should be mentioned as follows: a small number of the nonprecipitating cloud profiles are possibly

neglected in the statistical analysis. Based on the radar profile classification method in Section 2.3, nonprecipitating cloud profiles are determined by minutely rain rate. Therefore, six adjacent cloud profiles in one minute are classified as precipitating cloud profiles or non-precipitating cloud profiles. Therefore, a small quantity of nonprecipitating cloud profiles are out of the statistical analysis, when short-time rainfall occurs in less than one minute. Furthermore, previous analysis of the International Satellite Cloud Climatology Project (ISCCP) data revealed that regional differences in global cloud properties are closely related to the dynamic effects of thermodynamic and microphysical processes within clouds [61]. In this paper, the present findings concentrate on the macroscopic characteristics of the clouds on the ESTP, such as cloud occurrence frequency, radar reflectivity factor, CBH, CTH, and cloud thickness. To deeply investigate the regional cloud properties on the ESTP, more microphysical characteristics of clouds will be studied in further work. Studies about precipitating clouds on the ESTP by combining multisource observations (e.g., the space-borne active Ka/Ku-band radars [62]) will also be carried out in the future.

5. Conclusions

To better understand the cloud physical properties in the critical region of the TP, field observations on the ESTP were launched by the Institute of Heavy Rain, China Meteorological Administration, in 2019. This study explored the nonprecipitating cloud climatological characteristics across the ESTP using continuous Ka-MMCR observations collected in 2019 in four sites. For the first time, regional cloud vertical structures and diurnal variations on the ESTP were statistically analyzed in detail. The main conclusions are as follows.

Cloud occurrence frequency obtained from the Ka-MMCR measurements at GZ, LT, DC, and JL from 5 June to 20 August 2019, were compared. In general, the distribution of hydrometeor exhibits two peaks in summer on the ESTP. The first peak is located at 7–9 km, with a maximum occurrence frequency of 15% in the JL. The second peak is located at 2–4 km, with the maximum occurrence frequency of ~20% in the DC and JL. The maximum occurrence frequency throughout the day in the DC, JL, LT, and GZ are 78%, 70%, 55%, and 50%, respectively. Generally, cloud occurrence frequency of the ESTP increases rapidly in the afternoon (1300–1800 LT), and decreases slowly in the morning (0000–0500 LT), then minimizes around 1030 LT. In the DC, the occurrence frequency presents larger values (2%) from 1200 LT to 1800 LT at 2–4 km. In contrast, the occurrence frequency in the JL shows an increase from 2000 LT to midnight in the upper troposphere (7–11 km).

In the terms of the distributions of Z_e, nonprecipitating clouds on the ESTP present the mean values of reflectivity factors from −25 dBZ to −7 dBZ in the vertical direction. For mixed-phase clouds, the values of Z_e show a rapid increase at ~9 km, and maximize (−5–0 dBZ) at 5–7 km, then sequentially decrease downwards to ~3 km. Compared to other sites, clouds in the GZ are much weaker, with the maximum of mean Z_e with ~−5 dBZ. During the day, the values of Z_e increase from the afternoon (1300 LT), and maximize in the late evening. Among the four sites, stronger radar echoes occur most frequently in the LT, with the maximum Z_e (10 dBZ) at 5–7 km. A small number of strong radar echoes occur at midnight (0000–0100 LT) in the JL, with the maximum Z_e of 10 dBZ.

A characteristic bimodality of the cloud base height and top height for single-layer, double-layer, and triple-layer clouds was observed on the ESTP. Importantly, the main peak (1–4 km) location of base height of the lowest layer clouds in the GZ is higher by 1 km than other sites, while the main peak (7–10 km) location of base height of the highest layer clouds in the JL is higher by 1 km than other sites. For cloud top heights, the main peak (4.5–5 km) of the GZ is located higher than in other sites. The secondary peak of top heights in the JL is located at ~10 km, and is also apparently higher than in other sites. In addition, the ESTP is dominated by thin clouds with thicknesses of 200–400 m. Low clouds occur most frequently in the DC (46%), JL (39%), and LT (38%), respectively. The occurrence frequency of high clouds presents a larger value of 33% in the JL. In contrast, middle clouds

dominate in the GZ with 38% occurrence frequency. The four-site observations show that cloud base height, top height, and thicknesses increase significantly in the afternoon due to the convection on the ESTP in summer. Higher top heights occur more frequently at midnight and early morning in the JL due to its mountain-valley terrain.

Author Contributions: Conceptualization, R.W.; methodology, J.Z.; investigation, X.W.; resources, L.Y.; data curation, G.X.; writing—original draft preparation, X.W.; writing—review and editing, X.W.; visualization, J.Q.; supervision, R.W. All authors have read and agreed to the published version of the manuscript.

Funding: This work was supported by the Mountainous Sudden Rainstorm Integrated Observations in the Western China MOSRIO (Grant No. 2018YFC1507201), the National Natural Science Foundation of China (Grant No. 41620104009), the foundation of Key Laboratory of Atmosphere Sounding, China Meteorological Administration (U2021M06), the foundation of Heavy Rain and Drought-Flood Disasters in Plateau and Basin Key Laboratory of Sichuan Province (SZKT202108), and the Science and Technology Foundation of Wuhan Meteorological Service (WH202112).

Data Availability Statement: Data used in this study can be requested from the authors under the research institute polices of the Institute of Heavy Rain, China Meteorological Administration, Wuhan.

Acknowledgments: We thankfully acknowledge the Ganzizhou Meteorological Service for providing material support during the field experiment.

Conflicts of Interest: The authors declare no conflict of interest.

References

1. Qiu, J. China: The third pole. *Nat. News* **2008**, *454*, 393–396. [CrossRef] [PubMed]
2. Liu, Y.; Bao, Q.; Duan, A.; Qian, Z.; Wu, G. Recent progress in the impact of the Tibetan Plateau on climate in China. *Adv. Atmos. Sci.* **2007**, *24*, 1060–1076. [CrossRef]
3. Michio, Y.N.; Li, C.F.; Song, Z.S. Seasonal heating of the Tibetan plateau and its effects on the evolution of the Asian summer monsoon. *J. Meteor. Soc. Jpn.* **1992**, *70*, 319–351.
4. Fujinami, H.; Yasunari, T. The effects of midlatitude wave over and around the Tibetan Plateau on submonthly variability of the East Asian summer monsoon. *Mon. Wea. Rev.* **2009**, *137*, 2286–2304. [CrossRef]
5. Fan, Y.Y.; Li, G.P.; Lu, H.G. Impacts of abnormal heating of Tibetan Plateau on Rossby wave activity and hazards related to snow and ice in South China. *Adv. Meteor.* **2015**, *2015*, 87847. [CrossRef]
6. Li, L.; Zhang, R.H.; Wen, M.; Duan, J.P. Development and eastward movement mechanism of the Tibetan Plateau vortices moving off the Tibetan Plateau. *Clim. Dyn.* **2019**, *52*, 4849–4859. [CrossRef]
7. Tan, L.; Cai, Y.; Cheng, H.; Edwards, L.R.; Lan, J.; Zhang, H.; Li, D.; Ma, L.; Zhao, P.; Gao, Y. High resolution monsoon precipitation changes on southeastern Tibetan Plateau over the past 2300 years. *Quat. Sci. Rev.* **2018**, *195*, 122–132. [CrossRef]
8. Luo, Y.L.; Zhang, R.H.; Qian, W.M.; Luo, Z.Z.; Hu, X. Intercomparison of Deep Convection over the Tibetan Plateau–Asian Monsoon Region and Subtropical North America in Boreal Summer Using CloudSat/CALIPSO Data. *J. Clim.* **2011**, *24*, 2164–2177. [CrossRef]
9. Qie, X.S.; Wu, X.K.; Yuan, T.; Bian, J.C.; Lu, D.R.S. Comprehensive Pattern of Deep Convective Systems over the Tibetan Plateau–South Asian Monsoon Region Based on TRMM Data. *J. Clim.* **2014**, *27*, 6612–6626. [CrossRef]
10. Yan, Y.F.; Liu, Y.M. Vertical structures of convective and stratiform clouds in boreal summer over the Tibetan Plateau and its neighboring regions. *Adv. Atmos. Sci.* **2019**, *36*, 1089–1102. [CrossRef]
11. Zhang, F.; Yu, Q.R.; Mao, J.L.; Dan, C.; Wang, Y.Y.; He, Q.S.; Cheng, T.T.; Chen, C.H.; Liu, D.W.; Gao, Y.P. Possible mechanisms of summer cirrus clouds over the Tibetan Plateau. *Atmos. Chem. Phys.* **2020**, *20*, 11799–11808. [CrossRef]
12. Yu, L.; Fu, Y.F.; Yang, Y.; Pan, X.; Tan, R. Trumpet-shaped topography modulation of the frequency, vertical structures, and water path of cloud systems in the summertime over the southeastern Tibetan Plateau: A perspective of daytime–nighttime differences. *J. Geophys. Res. Atmos.* **2020**, *125*, e2019JD031803. [CrossRef]
13. Chen, D.D.; Guo, J.P.; Wang, H.Q.; Li, J.; Min, M.; Zhao, W.H.; Yao, D. The cloud top distribution and diurnal variation of clouds over East Asia: Preliminary results from Advanced Himawari Imager. *J. Geophys. Res. Atmos.* **2018**, *123*, 3724–3739. [CrossRef]
14. Guo, J.P.; Liu, H.; Wang, F.; Huang, J.F.; Xia, F.; Lou, M.Y.; Wu, Y.R.; Jiang, J.H.; Xie, T.; Yung, Y.L.; et al. Three-dimensional structure of aerosol in China: A perspective from multi-satellite observations. *Atmos. Res.* **2016**, *178–179*, 580–589. [CrossRef]
15. Gray, W.M.; Jacobson, R.W. Diurnal variation of deep cumulus convection. *Mon. Wea. Rev.* **1977**, *105*, 1171–1188. [CrossRef]
16. Hendon, H.; Woodberry, K. The diurnal cycle of tropical convection. *J. Geophys. Res.* **1993**, *98*, 162623–162637. [CrossRef]
17. Fu, Y.F.; Liu, G.S. Possible misidentification of rain type by TRMM PR over Tibetan Plateau. *J. Appl. Meteorol. Climatol.* **2007**, *46*, 667–672. [CrossRef]

18. Liu, B.; Huo, J.; Lu, D.R.; Wang, X. Assessment of FY-4A and Himawari-8 cloud top height retrieval through comparison with ground-based millimeter radar at sites in Tibet and Beijing. *Adv. Atmos. Sci.* **2021**, *38*, 1334–1350. [CrossRef]
19. Zhang, J.J.; Zhu, B.Z.; Zhu, F.K. *Tibetan Plateau Meteorological Progresses*; Science Press: Beijing, China, 1988; p. 268. (In Chinese)
20. Zhou, M.Y.; Xu, X.D.; Bian, L.G.; Chen, J.Y.; Liu, H.Z.; Zhang, H.S.; Li, S.M. *The Observation, Diagnosis and Dynamics of the Atmospheric Boundary over the Tibetan Plateau*; Meteorological Press: Beijing, China, 2000; 125p. (In Chinese)
21. Zhao, P.; Xu, X.; Chen, F.; Guo, X.; Zheng, X.; Liu, L.; Hong, Y.; Li, Y.; La, Z.; Peng, H.; et al. The Third Atmospheric Scientific Experiment for understanding the Earth–atmosphere coupled system over the Tibetan Plateau and its effects. *Bull. Amer. Meteor. Soc.* **2018**, *99*, 757–776. [CrossRef]
22. Zhao, C.F.; Liu, L.P.; Wang, Q.Q.; Qiu, Y.M.; Wang, Y.; Wu, X.L. MMCR-based characteristic properties of non-precipitating cloud liquid droplets at Naqu site over Tibetan Plateau in July 2014. *Atmos. Res.* **2017**, *190*, 68–76. [CrossRef]
23. Wang, H.; Guo, X.L. Comparative Analyses of Vertical Structure of Deep Convective Clouds Retrieved from Satellites and Ground-Based Radars at Naqu over the Tibetan Plateau. *J. Meteorol. Res.* **2019**, *33*, 446–462. [CrossRef]
24. Liu, L.P.; Gao, W.H. Statistical Analysis of Microphysical and Dynamical Parameters for Clouds and Precipitation over Nauq Tibetan Plateau in Summertime Using Ka-band Cloud Radar. *Atmosphere* **2020**, *11*, 818. [CrossRef]
25. Uyeda, H.; Yamada, H.; Horikomi, J.; Shirooka, R.; Shimizu, S.; Liu, L.P.; Ueno, K.I.; Fujii, H.; Koike, T. Characteristics of Convective Clouds Observed by a Doppler Radar at Naqu on Tibetan Plateau during the GAME-Tibet IOP. *J. Meteorol. Soc. Jpn. Ser.* **2001**, *79*, 463–474. [CrossRef]
26. Ma, Y.M.; Yao, T.D.; Wan, J.M. Experimental study of energy and water cycle in Tibetan Plateau—The progress introduction on the study of GAME/Tibet and CAMP/Tibet. *Plateau Meteorol.* **2006**, *25*, 344–351. (In Chinese)
27. Chen, Y.L.; Zhang, A.Q.; Zhang, Y.H.; Cui, C.G.; Wan, R.; Wang, B.; Fu, Y.F. A heavy precipitation event in the Yangtze River Basin led by an eastward moving Tibetan Plateau cloud system in the summer of 2016. *J. Geophys. Res. Atmospheres* **2020**, *125*, e2020JD032429. [CrossRef]
28. Wan, X.; Xu, G.R.; Wan, R.; Wang, B.; Ren, J.; Luo, C. Vertical structure of non-precipitation cloud obtained from cloud radar observation at Ganzi in the eastern Qinghai-Tibet Plateau. *Torrent. Rain Dis.* **2020**, *39*, 442–450. (In Chinese)
29. Fu, S.M.; Mai, Z.; Sun, J.H.; Li, W.L.; Ding, Y.; Wang, Y.Q. Impacts of convective activity over the Tibetan Plateau on plateau vortex, southwest vortex, and downstream precipitation. *J. Atmos. Sci.* **2019**, *76*, 3803–3830. [CrossRef]
30. Liu, L.P.; Zheng, J.F. Algorithms for Doppler Spectral Density Data Quality Control and Merging for the Ka-Band Solid-State Transmitter Cloud Radar . *Remote Sens.* **2019**, *11*, 209. [CrossRef]
31. Clothiaux, E.E.; Ackerman, T.P.; Mace, G.G.; Moran, K.P.; Marchand, R.T.; Miller, M.A.; Martner, B.E. Objective determination of cloud heights and radar reflectivities using a combination of active remote sensors at the ARM CART sites. *J. Appl. Meteorol.* **2000**, *39*, 645–665. [CrossRef]
32. Geerts, B.; Miao, Q. The use of millimeter Doppler radar echoes to estimate vertical air velocities in the fair-weather convective boundary layer. *J. Atmos. Ocean. Technol.* **2005**, *22*, 225–246. [CrossRef]
33. Görsdorf, U.; Lehmann, V.; Bauer-Pfundstein, M.; Peters, G.; Vavriv, D.; Vinogradov, V.; Volkov, V. A 35-GHz polarimetric Doppler radar for long-term observations of cloud parameters-description of system and data processing. *J. Atmos. Oceanic Technol.* **2015**, *32*, 675–690. [CrossRef]
34. Zheng, J.F.; Liu, L.P.; Zeng, Z.M.; Xie, X.; Wu, J.; Feng, K. Ka-band millimeter wave cloud radar data quality control. *J. Infrared Millim. Waves* **2016**, *35*, 748–757. (In Chinese)
35. Moran, K.P.; Martner, B.E.; Post, M.J.; Kropfli, R.A.; Welsh, D.C.; Widener, K.B. An unattended cloud-profiling radar for use in climate research. *Bull. Am. Meteorol. Soc.* **1998**, *79*, 443–455. [CrossRef]
36. Hollars, S.; Fu, Q.; Comstock, J.; Ackerman, T. Comparison of cloud-top height retrievals from ground-based 35 GHz MMCR and GMS-5 satellite observations at ARM TWP Manus site. *Atmos. Res.* **2004**, *72*, 169–186. [CrossRef]
37. Kollias, P.; Clothiaux, E.E.; Miller, M.A.; Albrecht, B.A.; Stephens, G.L.; Ackerman, T.P. Millimeter-wavelength radar: New frontier in atmospheric cloud and precipitation research. *Bull. Am. Meteorol. Soc.* **2007**, *88*, 1608–1624. [CrossRef]
38. Oh, S.B.; Kim, Y.H.; Kim, K.H.; Cho, C.H.; Lim, E. Verification and correction of cloud base and top height retrievals from Ka-band cloud radar in Boseong, Korea. *Adv. Atmos. Sci.* **2016**, *33*, 73–84. [CrossRef]
39. Liu, L.P.; Zheng, J.F.; Ruan, Z.; Cui, Z.H.; Hu, Z.Q.; Wu, S.H.; Dai, G.Y.; Wu, Y.H. The preliminary analyses of the cloud properties over the Tibetan Plateau from the field experiments in clouds precipitation with the various radars. *Acta Meteorol. Sin.* **2015**, *73*, 635–647. (In Chinese)
40. Li, G.P. *Dynamic Meteorology of the Tibetan Plateau*; China Meteorological Press: Beijing, China, 2021. (In Chinese)
41. Liu, Y.J.; Ding, Y.H. Analysis of Basic Features of the Onset of the Asian Summer Monsoon. *J. Meteorol. Res.* **2007**, *21*, 257–276.
42. Wang, Y.; Wang, C. Features of clouds and convection during the pre- and post-onset periods of the Asian summer monsoon. *Theor. Appl. Climatol.* **2006**, *123*, 551–564. [CrossRef]
43. Reiter, E.R.; Gao, D.Y. Heating of the Tibet Plateau and movements of the South Asian high during spring, Mon. *Weather. Rev.* **1982**, *110*, 1694–1711. [CrossRef]
44. Wu, G.X.; Liu, Y.M.; Wang, T.M.; Wan, R.J.; Liu, X.; Li, W.P.; Wang, Z.Z.; Zhang, Q.; Duan, A.M.; Liang, X.Y. The influence of the mechanical and thermal forcing of the Tibetan Plateau on the Asian climate. *J. Hydrometeorol.* **2007**, *8*, 770–789. [CrossRef]
45. Li, Y.; Zhang, M. Cumulus over the Tibetan Plateau in the summer based on CloudSat–CALIPSO data. *J. Clim.* **2016**, *29*, 1219–1230. [CrossRef]

46. Bouniol, D.; Couvreux, F.; Kamsu-Tamo, P.; Leplay, M.; Guichard, F.; Favot, F.; O'Connor, E.J. Diurnal and Seasonal Cycles of Cloud Occurrences, Types, and Radiative Impact over West Africa. *J. Appl. Meteorol. Climatol.* **2012**, *51*, 534–553. [CrossRef]
47. Zhou, Z.R.; Wang, G.L.; Zhaxi, S.L. Cloud vertical structure measurements from a ground-based cloud radar over the southeastern Tibetan Plateau. *Atmos. Res.* **2021**, *258*, 105629. [CrossRef]
48. Richard, J.D.; Dušan, S.Z. *Doppler Radar and Weather Observations*, 2nd ed; Dover Publications, Inc.: Mineola, NY, USA, 2006.
49. Rogers, R.R.; Yau, M.K. *A Short Course in Cloud Physics*; Butterworth-Heinemann, Burlington: Oxford, UK, 1989; 82p.
50. Zhang, Y.; Zhou, Q.; Lv, S.S.; Jia, S.Z.; Tao, F.; Chen, D.D.; Guo, J.P. Elucidating cloud vertical structures based on three-year Ka-band cloud radar observations from Beijing, China. *Atmos. Res.* **2019**, *222*, 88–99. [CrossRef]
51. Wu, C.; Liu, L.P.; Zhai, X.C. The Comparison of Cloud Base Observations with Ka-Band Solid-State Transmitter-Based Millimeter Wave Cloud Radar and Ceilometer in Summer over Tibetan Plateau. *Chin. J. Atmos. Sci.* **2017**, *41*, 659–672. (In Chinese)
52. Yan, Y.F.; Liu, Y.M.; Lu, J.H. Cloud vertical structure, precipitation, and cloud radiative effects over Tibetan Plateau and its neighboring regions. *J. Geophys. Res. Atmos.* **2016**, *121*, 5864–5877. [CrossRef]
53. Wang, H.; Luo, Y.L.; Zhang, R.H. Analyzing seasonal variation of clouds over the Asian monsoon regions and the Tibetan Plateau region using CloudSat/CALIPSO data. *Chin. J. Atmos. Sci.* **2011**, *35*, 1117–1131. (In Chinese)
54. World Meteorological Organization. *International Cloud Atlas: Abridged atlas*; WMO: Geneva, Switzerland, 1956.
55. Bhatt, B.C.; Nakamura, K. A climatological-dynamical analysis associated with precipitation around the southern part of the Himalayas. *J. Geophys. Res.* **2006**, *111*, D02115. [CrossRef]
56. Zhang, Y.; Zhang, L.J.; Guo, J.P.; Feng, J.M.; Cao, L.J.; Wang, Y.; Zhou, Q.; Li, L.X.; Li, B.; Xu, H.; et al. Climatology of cloud-base height from long-term radiosonde measurements in China. *Adv. Atmos. Sci.* **2018**, *35*, 158–168. [CrossRef]
57. Wu, G.; Liu, Y.; He, B.; Bao, Q.; Duan, A.; Jin, F.F. Thermal controls on the Asian summer monsoon. *Sci. Rep.* **2012**, *2*, 404. [CrossRef] [PubMed]
58. Duan, A.M.; Wu, G.X. Role of the Tibetan Plateau thermal forcing in the summer climate patterns over subtropical Asia. *Clim. Dyn.* **2005**, *24*, 793–807. [CrossRef]
59. Cai, H.K.; Feng, X.; Chen, Q.L.; Sun, Y.; Wu, Z.M.; Tie, X. Spatial and Temporal Features of the Frequency of Cloud Occurrence over China Based on CALIOP. *Adv. Meteorol.* **2017**, *2017*, 4548357. [CrossRef]
60. Guo, J.H.; Xue, H.W.; Liu, X.Y. Characteristics of Cloud Occurrence Frequency and Cloud Base Height in Summer over Beijing. *Acta Sci. Nat. Univ. Pekin.* **2015**, *51*, 718–724. (In Chinese)
61. Ding, S.G.; Zhao, C.S.; Shi, G.Y.; Wu, C.A. Analysis of global total cloud amount variation over the past 20 years. *J. Appl. Meteorol. Sci.* **2005**, *16*, 670–677. (In Chinese)
62. Wang, J.; Houze, R.A.; Fan, J.; Brodzik, S.R.; Feng, Z.; Hardin, J.C. The Detection of Mesoscale Convective Systems by the GPM Ku-Band Spaceborne Radar. *J. Meteorol. Soc. Jpn. Ser.* **2019**, *97*, 1059–1073. [CrossRef]